

A Major Geoeffective CME from NOAA 12371: Initiation, CME–CME Interactions, and Interplanetary Consequences

Bhuwan Joshi¹  · M. Syed Ibrahim¹ ·
A. Shanmugaraju² · D. Chakrabarty³

Received: 24 August 2017 / Accepted: 5 July 2018 / Published online: 20 July 2018
© Springer Nature B.V. 2018

Abstract In this article, we present a multi-wavelength and multi-instrument investigation of a halo coronal mass ejection (CME) from active region NOAA 12371 on 21 June 2015 that led to a major geomagnetic storm of minimum Dst = −204 nT. The observations from the *Atmospheric Imaging Assembly* onboard the *Solar Dynamics Observatory* in the hot EUV channel of 94 Å confirm the CME to be associated with a coronal sigmoid that displayed an intense emission ($T \sim 6$ MK) from its core before the onset of the eruption. Multi-wavelength observations of the source active region suggest tether-cutting reconnection to be the primary triggering mechanism of the flux rope eruption. Interestingly, the flux rope eruption exhibited a two-phase evolution during which the “standard” large-scale flare reconnection process originated two composite M-class flares. The eruption of the flux rope is followed by the coronagraphic observation of a fast, halo CME with linear projected speed of 1366 km s^{−1}. The dynamic radio spectrum in the decameter–hectometer frequency range reveals multiple continuum-like enhancements in type II radio emission which imply the interaction of the CME with other preceding slow speed CMEs in the corona within ≈ 10 –90 R_⊙. The scenario of CME–CME interaction in the corona and interplanetary medium is further confirmed by the height–time plots of the CMEs occurring during 19–21 June. *In situ* measurements of solar wind magnetic field and plasma parameters at 1 AU exhibit two distinct magnetic clouds, separated by a magnetic hole. Synthesis of near-Sun observations, interplanetary radio emissions, and *in situ* measurements at 1 AU reveal complex processes of CME–CME interactions right from the source active region to the corona and interplanetary medium that have played a crucial role towards the large enhancement of the geoeffectiveness of the halo CME on 21 June 2015.

Keywords Coronal mass ejections · Flares · Magnetic reconnection · CME–CME interaction · Magnetic clouds

✉ B. Joshi
bhuwan@prl.res.in

¹ Udaipur Solar Observatory, Physical Research Laboratory, Udaipur 313004, India

² Department of Physics, Arul Anandar College, Karumathur, Madurai 625514, India

³ Space and Atmospheric Sciences Division, Physical Research Laboratory, Ahmedabad 380009, India

1. Introduction

Solar flares and coronal mass ejections (CMEs) are the most energetic explosions in our solar system. Flares are characterized by a sudden catastrophic release of energy in the solar atmosphere. In tens of minutes, energy in excess of 10^{32} erg is released (see the review by Benz, 2017). CMEs refer to large-scale eruptions of plasma and magnetic field that erupt from the Sun and propagate into the interplanetary space with velocities from tens of km s^{-1} up to 3000 km s^{-1} (see the review by Schmieder, Aulanier, and Vršnak, 2015). The high radiation, fast particles and magnetic field brought by flares and CMEs cause severe space weather disturbances. Although most of the major flares are associated with CMEs, the relationship between the two phenomena is still not fully understood. It is generally accepted that magnetic reconnection plays a major role in the initiation and early evolution of flares as well as CMEs. Thus, investigation of the characteristics of CMEs, such as their source region properties, initiation and propagation are crucial to better understand the cause of solar activity and space weather phenomena.

Solar flares occur in solar active regions consisting of a distribution of sunspots of opposite magnetic polarities in the photosphere which are enveloped by large overlying coronal loops. The standard flare model provides a conceptual framework to understand the relationship between solar flares and filament eruptions (*e.g.* Kopp and Pneuman, 1976). According to this model, the beginning of the eruption process involves the expansion of a filament from the core of the active region. Thus, the activation of the filament or its associated hot channel – identified as the flux rope structure (*e.g.* Cheng *et al.*, 2013, 2014b) – can be regarded as the earliest signature for a CME (*e.g.* Joshi *et al.*, 2017). In the flux rope interpretation of a filament, we consider the filament to be one observable part of a larger magnetic structure that is capable of storing magnetic energy to drive eruptions (see, *e.g.*, Gibson and Fan, 2006; Krall and Sterling, 2007). The eruptive expansion of a filament causes the stretching of the overlying active region loops. The process progresses with the closing of the stretched field lines via magnetic reconnection which occurs at successive increasing heights in the corona (Shibata, 1999). Magnetic reconnection, occurring underneath the erupting filament, eventually leads to a series of complex multi-wavelength phenomena in the solar source region (see, *e.g.*, Joshi *et al.*, 2013). The eruptive filament, if it leaves the corona successfully against the overlying constraining magnetic fields and gravity of the Sun, forms the integral part of a coronal mass ejection (CME). In the classic three-part CME structure, the erupted filament is identified in the innermost region as the core of the CME. However, in most of cases, it has proven difficult to identify signatures of erupted filaments with *in situ* measurements of interplanetary CMEs (ICMEs) (Lepri and Zurbuchen, 2010; Vourlidas *et al.*, 2013). Furthermore, in the near-Sun region, it is still not clearly understood how magnetic reconnection and the overlying magnetic fields contribute toward controlling the kinematics of the CME. For example, observations indicate that filaments sometimes show eruption in several stages or undergo completely failed eruptions, *i.e.* eruption halts following the initial rapid activation of the filament (see, *e.g.*, Kushwaha *et al.*, 2015; Chandra *et al.*, 2017; Dhara *et al.*, 2017)

After the initial launch from the solar source region, the kinematic evolution of CMEs continuously changes as it propagates from the near-Sun region to the interplanetary medium. CMEs and their interplanetary counterparts (*i.e.* ICMEs) are the main source of major geomagnetic storms (see reviews by Zurbuchen and Richardson, 2006; Zhao and Dryer, 2014; Kilpua *et al.*, 2017). After take-off, ICMEs accelerate or decelerate depending on their speeds relative to the solar wind speed (see, *e.g.*, Shanmugaraju and Vršnak, 2014). Slow CMEs are accelerated by the solar wind, while the fast CMEs are decelerated. Therefore, the transit time of CMEs depends strongly on the state of the ambient solar wind. The

study of CME kinematics is utmost important in view of understanding space weather conditions. Notably, front-sided halo CMEs are thought to be potential candidates for producing strong geomagnetic storms. For the understanding of the Sun–Earth relationship in the context of space weather phenomena, it is essential to probe the individual flare–CME–ICME events which are associated with major geomagnetic storms (Syed Ibrahim, Shanmugaraju, and Bendict Lawrance, 2015). In order to improve space weather forecast, it is also essential to compare the model-based calculations of CME transit times with the actual transit time of ICMEs derived from solar observations and *in situ* measurements.

In this article, we discuss a major geoeffective CME that occurred on 21 June 2015. The source region of this CME was associated with eruptive and flaring activity in active region (AR) NOAA 12371 between 01:00 and 04:00 UT. A very interesting aspect of the source region of this CME was the occurrence of two successive solar eruptive flares of GOES class M2.0 and M2.6. We employ multi-wavelength, multi-instrument, and multi-point observations of the Sun and interplanetary medium to characterize various stages of the CME right from its initiation from the solar corona to its interplanetary propagation. The ICME corresponding to this solar eruption leads to a major geomagnetic storm of minimum Dst = −204 nT. In Section 2, we provide information on observational resources. The near-Sun characteristics of the CME are described in Section 3. The study of the CME driven interplanetary shock and magnetic cloud in the near-Earth region (1 AU) are given in Section 4. We discuss and interpret our observational results in Section 5. The concluding remarks are given in Section 6.

2. Observational Data

For this study, we have used solar and interplanetary data from the following sources:

- To investigate the source region of the CME, data from the *Atmospheric Imaging Assembly* (AIA: Lemen *et al.*, 2012) and the *Helioseismic Magnetic Imager* (HMI: Schou *et al.*, 2012) onboard the *Solar Dynamics Observatory* (SDO: Pesnell, Thompson, and Chamberlin, 2012) are used. We have analyzed EUV images of the Sun taken from the 94 Å filter of AIA which is sensitive to plasma at high temperature (~ 6 MK). The white-light and magnetogram images from HMI provide the photospheric view of the active region.
- The H α observations from the Global Oscillation Network Group (GONG¹) are used to infer the chromospheric changes during the eruption.
- The data from the *Radio and Plasma Waves* experiment (WAVES) radio spectrograph on *Wind* spacecraft (Bougeret *et al.*, 1995) is used to study the radio and plasma wave phenomena in the near-Sun region.
- To study the CME dynamics in the near-Sun region, we have used white-light images from the *Large Angle Spectrometric Coronagraph* (LASCO: Brueckner *et al.*, 1995) onboard *Solar and Heliospheric Observatory* (SOHO).
- We have analyzed *in situ* interplanetary plasma and magnetic field parameters associated with the CME using multi-instrument data which are collectively available at the Coordinated Data Analysis Web (CDAWeb²).

¹<http://halpha.nso.edu/archive.html>

²<https://cdaweb.sci.gsfc.nasa.gov/index.html/>

3. Initiation and Early Evolution of the CME

3.1. Multi-Wavelength View of Source Region NOAA 12371

Active region (AR) NOAA 12371 appeared on the solar disk on 17 June 2015 at the heliographic location N11E66 with a simple β type magnetic configuration. The active region grew rapidly in terms of size as well as magnetic complexity and turned into $\beta\gamma\delta$ category on 19 June 2015. The solar and heliospheric activities reported in this article correspond to the major eruptive event in AR 12371 on 21 June 2015 when the mean location of the active region was N13E14. In Figure 1, we show the multi-wavelength view of the active region on the day of the reported activity. The intensity image from HMI/SDO clearly indicates leading and following sunspot groups. The leading sunspot group largely consists of a major sunspot of negative polarity, while the following group is a complex mixed polarity region (*cf.* Figures 1a–b). To compare the photospheric structure of the active region with the overlying chromospheric and coronal layers, we show $H\alpha$ and AIA 94 Å images of the active region in Figures 1c and 1d, respectively. The comparisons of $H\alpha$ filtergrams with HMI intensity and magnetogram images clearly reveal the presence of a long U-shaped filament channel that extends over different parts of the active region. The eastern edge of the filament channel originates from the following sunspot group while its western edge bends around the leading sunspot group.

On 21 June 2015, AR 12371 underwent significant eruptive and flaring activity. In Figure 2, we show the evolution of the solar X-ray flux observed by the *Geostationary Operational Environmental Satellite* (GOES) during 00:00–05:30 UT. We find that the GOES flux exhibited two evolutionary phases during this interval. The GOES flux started to build up from 01:02 UT onwards, peaked at 01:42 UT, and decayed afterwards. After reaching a minimum at \approx 02:00 UT, the X-ray flux further increased and had a second peak at 02:36 UT. The first and second peaks correspond to flares of class M2.0 and M2.6, respectively. Both flares occurred at almost the same locations (N12E13 and N12E16) and were also similar in terms of GOES peak flux. However, the detailed $H\alpha$ imaging showed morphological differences between the two events in terms of shape and extension of flare ribbons (Section 3.2). Therefore, it would be appropriate to call the two events as nearly homologous. The flares are associated with a fast halo CME. The AIA 94 Å images during the pre-flare interval (Figure 1c) clearly show that the activity site is enveloped by twisted hot coronal loops that collectively present an S-shaped or sigmoidal structure. Notably, the most intense emission from the sigmoid originates from a compact region which is spatially associated with the trailing part of the AR (*cf.* Figure 1a–c) that exhibits much magnetic complexity in the photosphere than the rest of the AR (Figure 1a). We call this region as the core of the sigmoid which essentially represents the upper-most part of the loops that form it. Further, the intense brightening of the core region indicates localized pre-flare heating.

3.2. $H\alpha$ Observations: Filament Eruption and Flare Ribbons

To investigate the source region of the CME, we thoroughly examined the 1-min cadence $H\alpha$ filtergrams from GONG. A few representative filtergrams showing the important phases of the eruptive activity are shown in Figure 3. $H\alpha$ images clearly reveal that during the first flare (GOES M2.0 flare from 01:02–02:00 UT), the main source of chromospheric emission lies close to the following part of the active region in the form of flare ribbons at opposite sides of the filament (see the region enclosed by the circle in Figure 3b). The ribbon brightenings grew with time but their spatial extension remained the same. Afterwards, we note

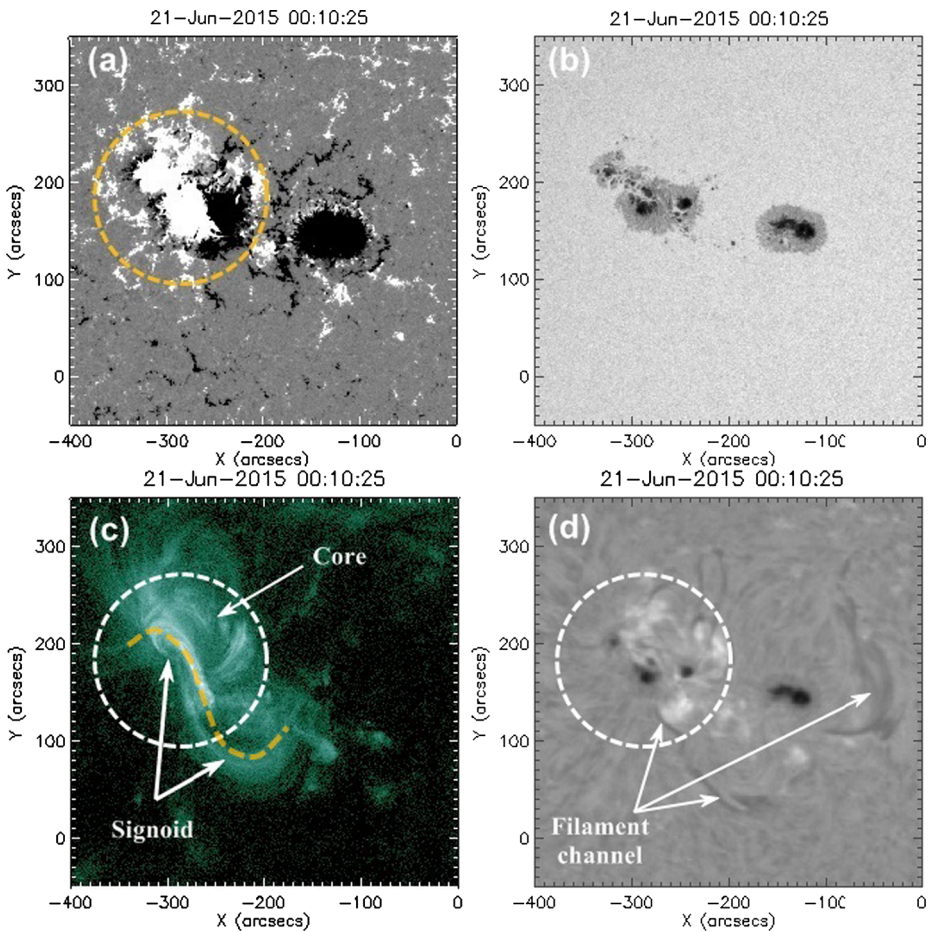


Figure 1 Multi-wavelength view of AR NOAA 12371 showing the environment where eruptive flares occurred from 01:00–05:00 UT on 21 June 2015. **(a)** and **(b)**: HMI white-light image and magnetogram of the AR 12371 showing the distribution of sunspots and their magnetic polarities, respectively. *White and black colors* in the HMI magnetogram indicate positive and negative magnetic polarity regions, respectively, in the photosphere. **(c)**: AIA 94 Å image of the AR prior to the eruption, showing hot coronal loops that are twisted to form an overall S-shape, *i.e.* a sigmoidal structure. The sigmoid is shown by the *dashed yellow curve*. Panel **(d)**: GONG H α filtergram showing the chromospheric counterpart of the coronal sigmoidal region. We note a filament channel (marked by *arrows*) at the activity site which partially erupted in two stages during the homologous flares. The flux rope eruption is first triggered at the core of the sigmoid which is indicated by a *dashed circle* in **(a)**, **(c)**, and **(d)**.

the activation and subsequent eruption of the filament (shown by an arrow in Figure 3d). It is noteworthy that the filament did not completely erupt during the first flare. After 02:00 UT, we find the second stage of the eruption which led to further brightening of flare ribbons. It is important to note that the western flare ribbon underwent a more dynamic evolution during which it extended up to the following sunspot group (Figure 3h). This period corresponds to the second flare (GOES M2.6 flare during 02:06–03:02 UT). Furthermore, the western flare ribbon presented a semi-circular morphology which sustained till the late phases of the flare evolution (\approx 03:00 UT).

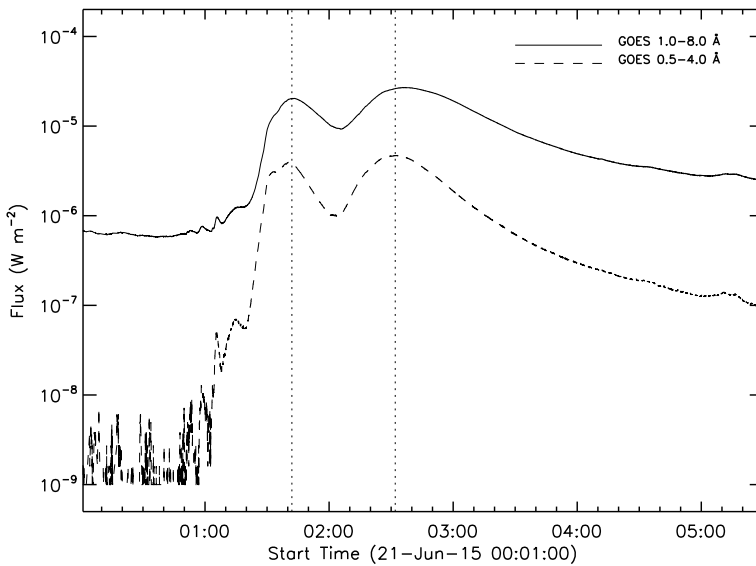


Figure 2 GOES light curves showing the evolution of homologous eruptive flares. *Solid and dashed lines* indicate X-ray flux in 1–8 Å and 0.5–4 Å wavelength bands which correspond to disk-integrated X-ray emission in the 1.5–12.5 keV and 3–25 keV energy range, respectively. *Vertical dotted lines* at 01:42 UT and 02:36 UT indicate peak phases of the M2.0 and M2.6 flares, respectively.

3.3. AIA 94 Å Imaging: Two-Phase Eruption of the Hot Flux Rope

To investigate the restructuring of the active region corona during the first and second flare, we analyze AIA 94 Å images. As noted earlier (see Figure 1; bottom panels), the active region consisted of a long filament channel in the chromosphere (see $H\alpha$ filtergrams), while hot, twisted loops existed in the overlying coronal layers. The sequence of AIA 94 Å images during the successive M-class flares (see Figure 2) reveals a two-step eruption process. The earliest signatures of eruption are identified in 94 Å images with the activation and successive rapid expansion of hot channel-like structures from low coronal heights. In order to show the progression of the erupting structures clearly, we plot AIA 94 Å running difference images in Figure 4. On the basis of the structure and morphological evolution of the expanding hot channels, we identify this feature as a magnetic flux rope (see, *e.g.*, Cheng *et al.*, 2013; Joshi *et al.*, 2007). The difference images clearly exhibit the two-phase eruption of the flux rope. During the first phase (Figure 4a–d), the flux rope erupted in north-east and south-west directions while during the second phase (Figure 4e–g), the flux rope eruption proceeded in north-east and south directions. After the eruption, we observe the growing structure of the closed post-flare loops (Figure 4h–i).

3.4. LASCO Observations: CME in the Near-Sun Environment

LASCO onboard SOHO images the white-light corona from $2 R_{\odot}$ to $30 R_{\odot}$. The C2 coronagraph covers a field of view of $2–6 R_{\odot}$, whereas the C3 coronagraph images the corona from $4–30 R_{\odot}$. According to LASCO CME catalogue,³ the filament eruption (see Section 3.2)

³https://cdaw.gsfc.nasa.gov/CME_list/

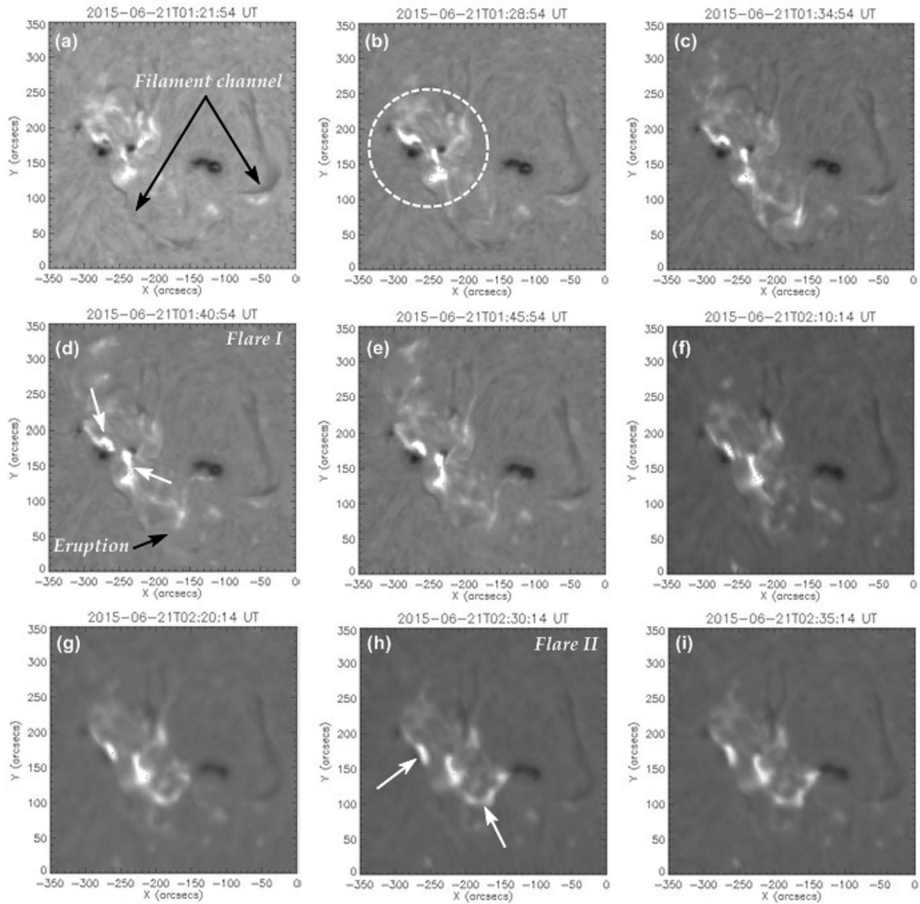


Figure 3 Representative $H\alpha$ filtergrams showing two stages of the filament eruption and subsequent flare emissions in AR NOAA 12371. (a)–(e): The first flare (M2.0) ribbons (shown by *arrows* in (d)) are shorter and located in a confined region (shown by the *dashed circle* in (b)), which lies within the bipolar magnetic region of the following sunspot group of AR (*cf.* Figure 1a). (f)–(i): The second flare (M2.6) ribbons exhibit an extended structure. (d) and (h) show the peak phases of the two flares.

led to a halo CME (Figure 5). The CME was first detected by LASCO C2 coronagraph at a height of $3.6 R_{\odot}$ on 21 June at 02:36 UT. The CME could be followed by the C3 coronagraph up to the height of $24.3 R_{\odot}$ at 05:30 UT. A linear fit to the CME height–time data indicated the CME to be a faster one with a speed of 1366 km s^{-1} . Here we note that, although the eruption from the source active region followed a two-phase evolution (see Sections 3.2 and 3.3), which resulted into two successive M-class flares (Figure 2), the coronagraphic images do not seem to contain signatures of two-phase eruptions. Thus, it seems that the two-phase eruption of the flux rope evolved into one CME structure at heights $\geq 2 R_{\odot}$.

We used the observed CME parameters from SOHO/LASCO to estimate the transit time of the CME from the Sun to the near-Earth region using CME arrival time prediction models. However, besides various CME parameters at the near-Sun region along with solar wind conditions, the actual CME arrival time at the near-Earth region also depends upon the interactions among CMEs traveling in the interplanetary medium. During such interactions,

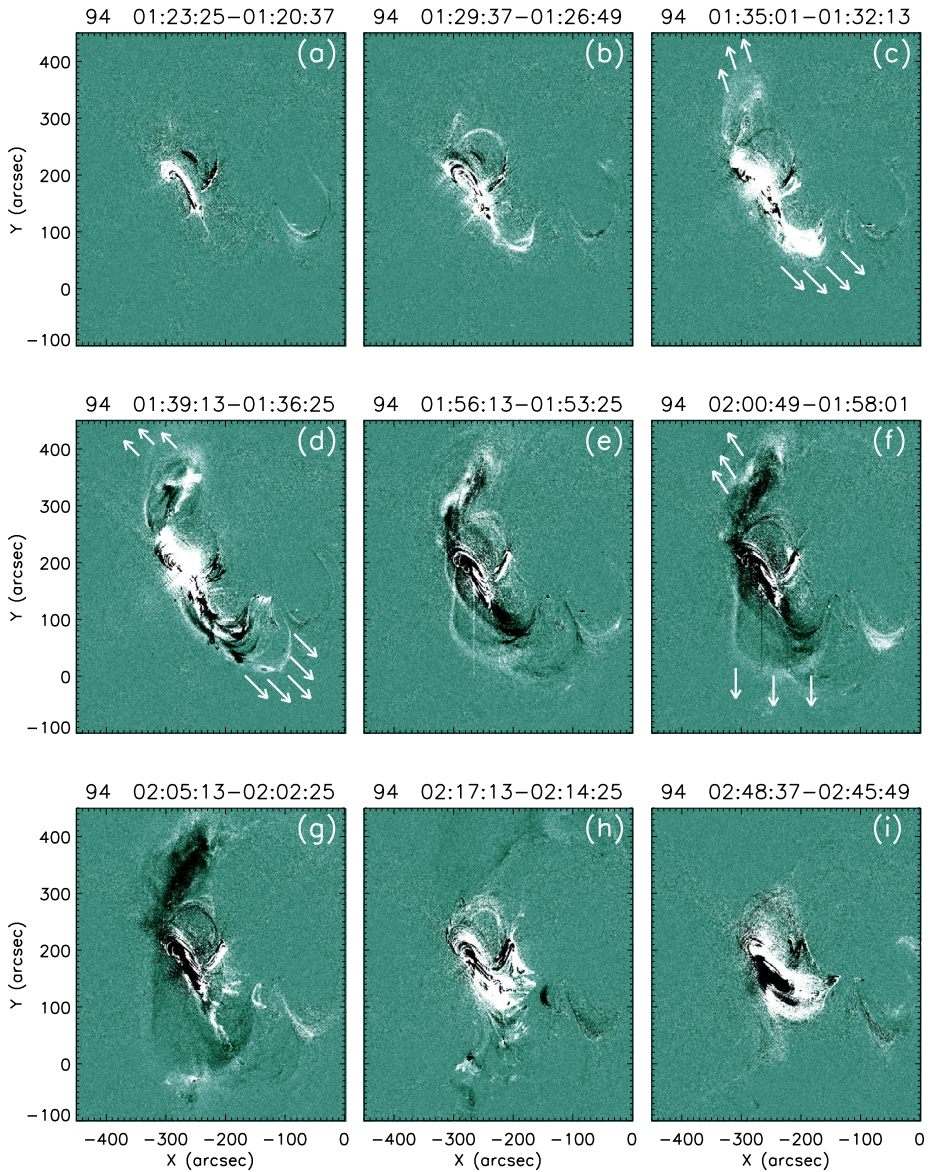


Figure 4 AIA 94 Å running difference images showing two distinct phases of the flux rope eruption from the sigmoidal active region (*cf.* (c)–(d) and (f)–(g)). Arrows are drawn in (c), (d), and (f) to indicate the structures and directions of the erupting flux rope. The timings of both images used to create the difference image are annotated at the top of each panel.

the primary CME overtakes one or more slower CMEs. In order to verify the possibility of CME–CME interactions, we examined the flare–CME events that occurred prior to and after the reported activity. In Table 1, we summarize various parameters of the CMEs that occurred during 19–21 June 2015. It is worth to mention that, for later CMEs (*i.e.* during 21–22 June), the LASCO observations show relatively slower events which cannot take

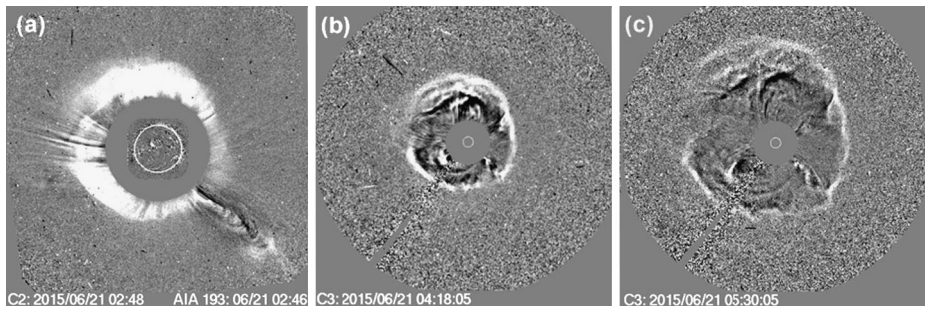


Figure 5 (a)–(c): Running difference images derived from LASCO C2 (panel a) and C3 (panels b–c) showing that the propagation of the halo CME originated from AR NOAA 12371 on 21 June 2015.

Table 1 Summary of the coronal mass ejections observed during 19–21 June 2015. The second column (*i.e.* date and time) gives the time of first appearance of the CME in LASCO C2. PA and AW denote position angle and angular width, respectively. The height–time plots of these CMEs (numbered from 1–9) are given in Figure 6.

No.	Date and time DD/MM – hh:mm UT	PA	AW (deg)	Linear speed (km s ⁻¹)	Acceleration (m s ⁻²)
1	19/06 – 06:42 UT	halo	360	584	19.5
2	19/06 – 18:00 UT	98	36	368	5.6
3	20/06 – 02:36 UT	228	33	360	13.4
4	20/06 – 07:36 UT	120	56	435	-6.4
5	20/06 – 11:00 UT	105	20	527	3.3
6	20/06 – 12:48 UT	39	32	409	8.7
7	20/06 – 15:36 UT	225	31	325	2.7
8	20/06 – 22:12 UT	227	31	118	14.6
9	21/06 – 02:36 UT	halo	360	1366	21.2

over the 21 June fast CME in the interplanetary medium. We find that on 20 June, the same active region produced two CME events from source locations N14E27 and N13E25 (events No. 3 and No. 4 in Table 1) which are associated with flares of class C2.3 and M1.0, respectively. The speeds of these CMEs within LASCO field of view (FOV) are estimated as 360 km s⁻¹ and 435 km s⁻¹. Both events have small angular widths. From the point of view of CME–CME interaction in the interplanetary medium, we note the occurrence of a more significant event of halo type at the location S21W27 on 19 June (event No. 1 in Table 1), *i.e.* ≈ 2 days before the event under investigation with a speed of 584 km s⁻¹. Apart from these most probable candidates for CME–CME interactions, we cannot rule out the possibility of interactions of the primary CME (*i.e.* the event under investigation) with other slower events that occurred in different active regions and locations during the previous 2–3 days. In Figure 6, we provide height–time plots for the CMEs that occurred during 19–21 June which can possibly interact while propagating in the corona and interplanetary medium. A comparison of height–time plots of the CMEs suggests a major possibility of interactions of the primary CME with the preceding ones in the height range of ≈ 10 –90 R_⊙. The height–time plots further suggest CME–CME interactions at very large distances from the Sun, even possibly close to 1 AU (*e.g.* see the height–time plots of event No. 1 and No. 9;

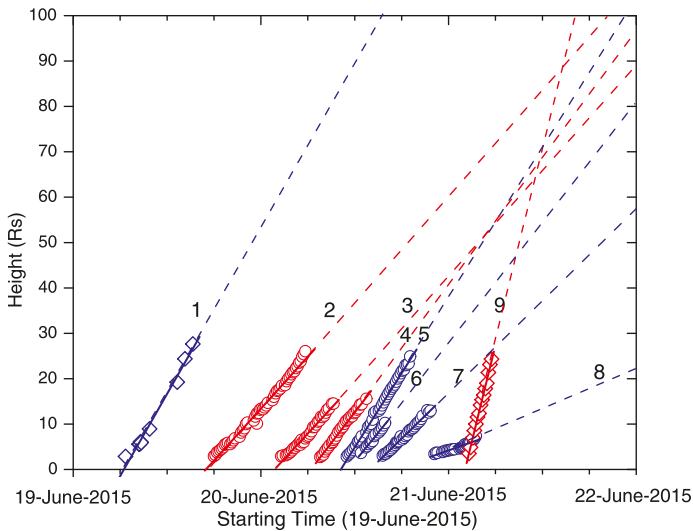


Figure 6 Height–time plots for the CMEs (numbered as 1–9) that occurred during 19–21 June 2015. The *solid lines* indicate linear fittings that are further extended up to $100 R_{\odot}$ (*dashed lines*) to speculate on the possibility of CME–CME interaction. *Diamond and circle symbols* indicate halo and non-halo CMEs, respectively. *Red plots* mark CMEs originated from the active region NOAA 12371 while *blue plots* mark events that are associated to other regions. The height–time plot labeled 9 denotes the primary CME of 21 June 2015, which is analyzed in this article.

Figure 6). We have further confirmed the interaction between the primary fast CME and preceding slow CMEs through the analysis of the radio spectrum observed with the *Radio and Plasma Wave Investigation* instrument (WAVES) onboard *Wind*.

3.5. Radio Dynamic Spectrum by *Wind*/WAVES

The radio dynamic spectrum obtained by *Wind*/WAVES showed a significant activity over a wide range of frequencies between 20 kHz and 14 MHz providing insight of the plasma and magnetic field processes driven by the flare and CME in the solar corona and beyond (Figure 7). The initial magnetic field line opening can be inferred from the type III burst at the time of the peak phase of the first event ($\approx 1:40$ UT, refer to Figure 2). Following this, two type III bursts occurred around 2:00 UT which confirms further opening of coronal magnetic fields in the wake of the onset of the second flare (see Figure 2) and simultaneous ejection of relativistic electron beams. The type II burst is observed in the decameter–hectometric (DH) spectrum at $\approx 2:30$ –3:10 UT in the frequency range of 5 MHz–1 MHz. Using this frequency range, corresponding heights are estimated using Leblanc’s density model (Leblanc, Dulk, and Bougeret, 1998) as ≈ 2.7 –6.3 R_{\odot} and the shock speed is determined as ≈ 1020 km s $^{-1}$. Note that this speed is close to the linear speed of the CME measured in the LASCO field of view as 1366 km s $^{-1}$. The occurrence of type III and onset of type II radio bursts provide the earliest signatures of the processes that lead to the CME initiation. The DH type II continues beyond 1.0 MHz to 0.2 MHz after 03:10 UT to $\gtrsim 8:00$ UT. The frequency range and duration of this type II implies a height range of ≈ 6.25 –26 R_{\odot} with a speed of ≈ 800 km s $^{-1}$. Also during this interval, strong patches of intensity enhancements in the type II radio emission are seen at around 4:00–5:30 UT within a frequency range of ≈ 1 –0.3 MHz. These intense patches reveal the interaction of

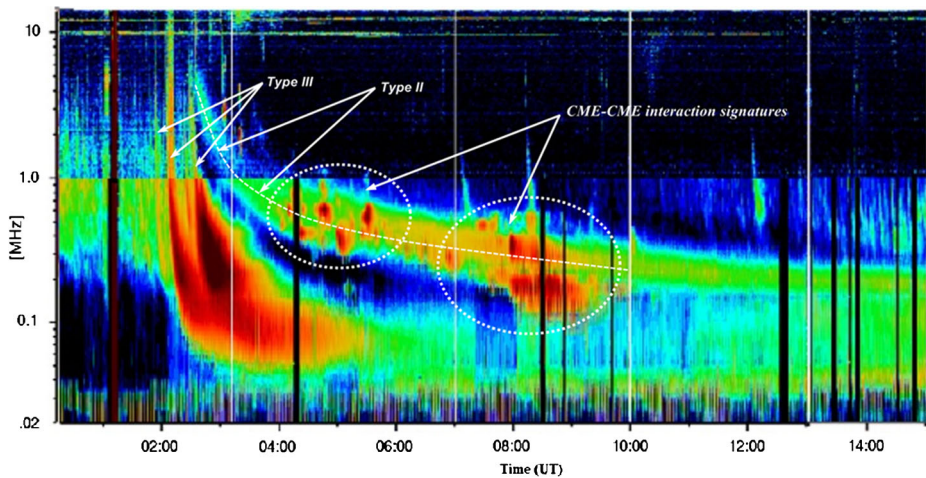


Figure 7 Solar dynamic radio spectrum obtained from *Wind*/WAVES in the frequency range of 20 kHz to 14 MHz, showing a wide range of radio activity associated with the CME on 21 June 2015 along with prominent signatures of CME–CME interactions.

the primary CME with previous CMEs at a height range of $\approx 6\text{--}17 R_{\odot}$. Moreover, we note very intense and relatively longer patches of enhancement in the intensity of the type II band in the frequency range $\approx 0.1\text{--}0.4$ MHz from $\approx 7:30\text{--}9:00$ UT that further points toward a CME–CME interaction. The interaction signatures observed in the radio dynamic spectra are consistent with the locations and timings of the CMEs that occurred during 19–21 June, described in Section 3.4. Further, the comparisons of CME height–time plots obtained from LASCO indicate the possibilities of CME–CME interactions well beyond *Wind*/WAVES observing frequencies.

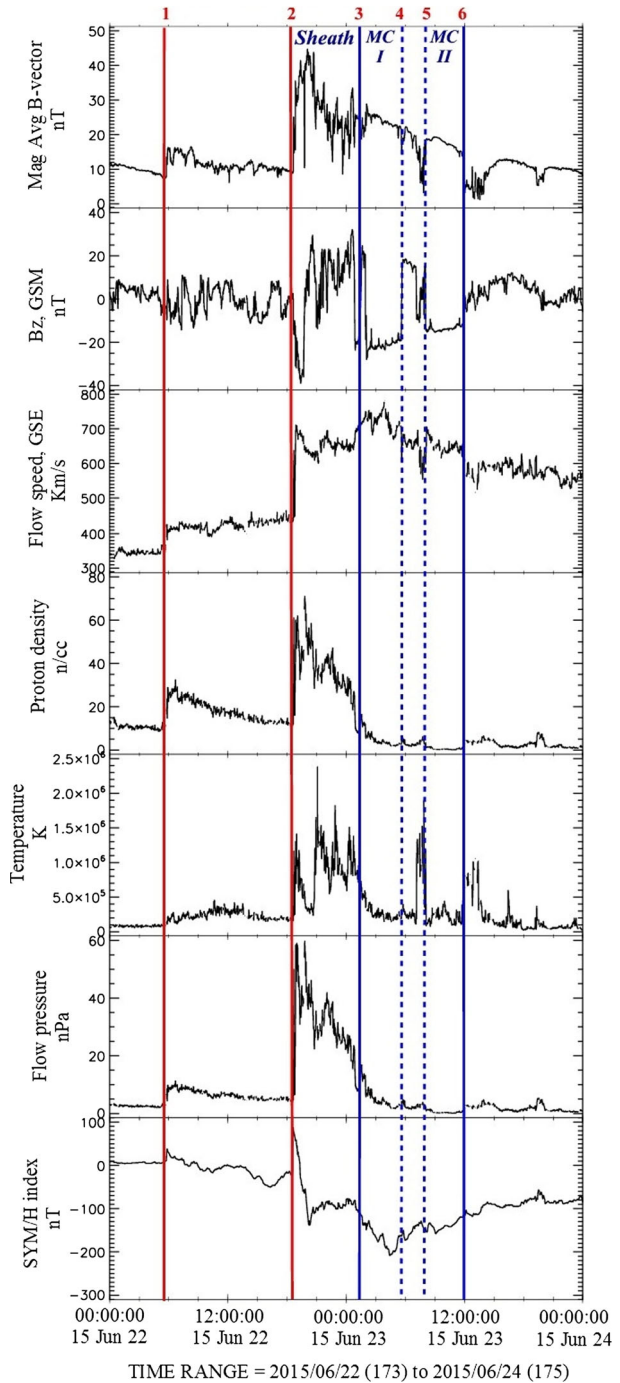
4. Near-Earth IP Shock and ICME

4.1. *In situ* Observations

In Figure 8, we present the interplanetary plasma and magnetic field parameters of the ambient solar wind and the CME-associated disturbances observed at 1 AU. These data sets have been obtained from the CDAWeb (see Section 2). These plots show variations of the total magnetic field strength, the z -component of the magnetic field, flow speed, proton density, proton temperature, flow pressure, SYMH index (*i.e.* high resolution Dst index). Note that the z -component of the magnetic field is shown in geocentric solar magnetospheric (GSM) coordinates while flow speed is given in geocentric solar ecliptic (GSE) coordinates.

Figure 8 illustrates the solar wind conditions prior to the shock, shocked plasma, and the CME driver gas. We find the first signature of shocked plasma just before $\approx 06:00$ UT on 22 June 2015 (indicated by a red vertical line numbered as 1). However, as seen from the plots, this shock is of low strength. The *in situ* measurements exhibit large and sudden fluctuations of all plasma and magnetic field parameters just after $\approx 18:00$ UT on 22 June 2015, evidencing the arrival of another distinctly different shock, moving ahead of a large CME structure. In the sheath of shocked plasma (see the region between the vertical lines 2 and 3), the magnetic field undergoes rapid oscillations. Following the sheath, we observe magnetic

Figure 8 *In situ* observations of interplanetary plasma and magnetic field parameters during 22–24 June 2015. From top to bottom: total magnetic field strength, the z -component of the magnetic field, flow speed, proton density, proton temperature, flow pressure, SYM/H index (*i.e.* high resolution Dst index). The vertical solid lines (lines 1 and 2) mark the arrival of shocks. We note that the intensity of shock 1 is significantly lower than that of shock 2 and it likely represents the disturbances caused by slow CMEs propagating ahead of the large halo CME on 21 June 2015. The shock 2 is associated with the arrival of the halo CME on 21 June 2015. The region between lines 2 and 3 represents the sheath of the CME which is followed by the magnetic cloud (MC) structures. The plasma and magnetic parameters exhibit a discontinuity during the passage of the MC (see the region between the vertical dashed lines, lines 4 and 5, which separates the MC into two parts (MC I and MC II).



cloud (MC) like features from $\approx 01:30$ – $06:00$ UT on 23 June 2015 (region between the vertical solid lines 3 and 6, top panel in Figure 8). As typically observed, the magnetic cloud region (*i.e.* ICME) is frequently identified with a reduction in the magnetic field variability (*i.e.* the relatively strong but smoothly decreasing field strength) along with lower proton temperature (Burlaga *et al.*, 1981). However, we find some irregularities in the variations of magnetic and plasma parameters within the passage of the MC and this interval is marked by the vertical dashed lines 4 and 5. Hence, we divide the MC structure into two parts: MC I and MC II in Figure 8 (top panel).

The bottom panel of Figure 8, shows the time evolution of the SYMH index. We find a small and gradual decline of the index following the arrival of shock 1 (see red vertical line just before $\approx 06:00$ UT on 22 June 2015). The SYMH index undergoes a brief episode of rapid enhancement around the arrival of the major shock (*i.e.* shock 2; see the red vertical line just after $\approx 18:00$ UT on 22 June 2015). This brief episode of SYMH enhancement is followed by a prolonged declining phase. Notably, the decay in the SYMH index is more prominent during the passage of the magnetic cloud (see MC I region in Figure 8). The index falls to a minimum value of -204 nT at $\approx 05:00$ UT on 23 June 2015 and, afterwards, it undergoes a recovery phase.

4.2. Comparisons with Model Predictions

We have used two CME and shock prediction models to estimate the arrival time of the ICME and interplanetary (IP) shocks at 1 AU: (1) the drag based model (Vršnak *et al.*, 2013), and (2) the empirical CME arrival model (Gopalswamy *et al.*, 2001a). Input parameters for both models are based on near-Sun measurements of the CME by LASCO onboard SOHO.

The drag based model (DBM) is built on the hypothesis that the driving Lorentz force, which launches a CME, ceases in the upper corona and that beyond a certain distance the dynamics becomes governed solely by the interaction of the ICME and the ambient solar wind. The input parameters of the DBM model are: the starting radial distance of the CME (r_o), the speed of the CME at r_o (v_o), the drag parameter (γ), and the asymptotic solar wind speed (w). Preferably, r_o should be around, or beyond, a radial distance of $r = 20 R_\odot$, so that the conditions $\gamma = \text{const.}$ and $w = \text{const.}$ are approximately fulfilled. According to LASCO observations, the CME is first detected in C2 FOV at a radial distance of $3.53 R_\odot$ at 02:36 UT and followed by C3 up to a height of $24.32 R_\odot$ at 05:30 UT. The second order polynomial fit to the CME height–time data shows the CME speed at $20 R_\odot$ to be 1434 km s^{-1} . The ambient solar wind speed is taken as 350 km s^{-1} , which is the average speed of the plasma flow, recorded *in situ*, before the shock 1 (see Figure 8). With these input parameters, the CME transit time, from its first detection on the Sun at $3.53 R_\odot$ to 1 AU, comes out to be 49.2 hours with an impact speed (at 1 AU) of 583 km s^{-1} .

The empirical CME arrival (ECA) model assumes that CMEs undergo an “effective” constant acceleration or deceleration process during their propagation outward. Usually, the effective acceleration will stop at a cessation distance (d_1) before 1 AU, then the CME propagates at a constant speed for the remaining distance $d_2 = 1 \text{ AU} - d_1$. Thus the transit time of the CME is $t = t_1 + t_2$, where t_1 is the time of travel up to d_1 and t_2 is the time of travel up to d_2 . Following Gopalswamy *et al.* (2001a), we have considered 0.7 AU as the acceleration cessation distance. Using an empirical relation between the CME acceleration and initial speed (Equation 4 in Gopalswamy *et al.*, 2001a), the effective CME acceleration from Sun to 0.7 AU is estimated as -5.2 m s^{-2} . This simplistic model gives the transit time for the CME-associated interplanetary shock of 40.1 hours. A summary of the CME-associated parameters from the observations and model predictions are given in Table 2.

Table 2 Summary of observed and computed parameters of the coronal mass ejection.

First detection	2:36 UT on 21 June 2015
Height of first detection	3.53 R_{\odot}
Linear speed (from LASCO observations)	1366 km s ⁻¹
Second order speed at final height	1477 km s ⁻¹
Second order speed at 20 R_{\odot}	1434 km s ⁻¹
Shock arrival at 1 AU	~ 18:00 UT on 22 June
ICME arrival at 1 AU	~ 01:30 UT on 23 June
Observed transit time for shock from first CME detection	39.4 hours
Observed transit time for ICME from first CME detection	46.9 hours
Predicted transit time from drag-based model (DBM)	49.2 hours
Predicted transit time from empirical CME arrival (ECA) model	40.1 hours

5. Summary

In this article, we study the initiation of the CME from NOAA 12371 on 21 June 2015 and its further consequences in the corona and interplanetary medium that led to a major geoeffective event on 23 June 2015 with minimum $Dst = -204$ nT. This highly geoeffective structure consisted primarily of the two CMEs that left the Sun on 19 June and 21 June and seemed to interact at larger distances in the interplanetary medium.

On 21 June 2015, AR 12371 had evolved into a magnetically complex $-\beta\gamma\delta$ type – active region and was located on the solar disk at N13E14. The multi-instrument observations from SDO (Figure 1) revealed a large system of coronal loops over the mixed magnetic polarity regions in the photosphere. The whole loop system, spreading from north-east to south-west, form an overall S-shape a coronal sigmoid. Sigmoid structures in active regions were first identified in soft X-ray images of the Sun (Manoharan *et al.*, 1996; Rust and Kumar, 1996). It was also found that sigmoidal active regions are prone to undergo more eruptions when compared to the non-sigmoidal regions (Canfield, Hudson, and McKenzie, 1999; Glover *et al.*, 2000). Many recent studies have confirmed that sigmoidal structures are not only associated with soft X-rays but are well observed in different EUV channels, mostly in hot channels, which provides evidence that coronal sigmoids exist over a wide range of temperatures (see, *e.g.*, Liu *et al.*, 2007; Cheng *et al.*, 2014a; Joshi *et al.*, 2017).

Using solar observations in $H\alpha$, we find that underneath the coronal sigmoid, a large twisted filament channel existed (*cf.* Figure 1c–d). The spatial association between the hot coronal sigmoid and the cool chromospheric filament has been recognized in several studies (see, *e.g.*, Pevtsov, 2002; Joshi *et al.*, 2017). The $H\alpha$ images show initial flare brightenings in the form of multiple, localized patches close to the filament (Figure 3a). This region lies underneath the core of the EUV sigmoid (marked in Figure 1c) from where the flux rope eruption initiated at low coronal heights. Considering the fact that EUV emission at 94 Å corresponds to hot plasma ($T \sim 6$ MK), we attribute the enhanced pre-flare emission from the core of the sigmoid along with the underlying localized $H\alpha$ brightenings as signatures of magnetic reconnection in the lower coronal and chromospheric region (see, *e.g.*, Joshi *et al.*, 2011; Bamba *et al.*, 2017). Further comparison of the location of the early eruption in $H\alpha$ and EUV images with the corresponding magnetogram reveal the destabilization of the flux rope to be associated with a magnetically bipolar region. These observations support the tether-cutting model (Moore and Roumeliotis, 1992; Moore *et al.*, 2001) as the triggering mechanism of the flux rope eruption.

GOES profiles (Figure 2) indicate the temporal evolution of energy release during the two successive flares. As evident from the sequence of H α images, the first M2.0 flare (01:02 UT–02:00 UT) is associated with the development of two closely situated flare ribbons at the eastern part of the active region (Figure 3b–d). Since flare ribbons represent the foot-points of the coronal loops involved in the coronal magnetic reconnection (Fletcher *et al.*, 2011), we propose that during the first flare, reconnection occurs in the core field region, *i.e.* field lines which are close to the polarity inversion line. The second flare (02:06 UT–03:02 UT) shows more extended flare ribbons (Figure 3e–i) which imply a second stage of magnetic reconnection in which field lines rooted at relatively larger distances from the polarity inversion line are involved.

The 94 Å AIA images reveal that the eruption proceeds in the form of high temperature, arc-like plasma structures from the active region corona in two steps (Figure 4). Based on many contemporary observations from SDO/AIA, we identify these arc-like moving features as magnetic flux ropes (Cheng *et al.*, 2011, 2013; Patsourakos, Vourlidas, and Stenborg, 2013; Nindos *et al.*, 2015; Joshi *et al.*, 2017). From the running difference images, it is evident that different portions of the flux rope erupted during the first and second flare. Furthermore, the erupting arc-like structures followed different directions during the first and second phases (see arrows showing the propagation of the flux rope in Figure 4c–d and f), *i.e.* the flux rope underwent an asymmetric eruption. During the activation of the flux rope, we observe the signatures of magnetic reconnection in the form of type III radio bursts (see types III at \approx 01:40 and \approx 02:00 UT; Figure 7) which imply opening of overlying magnetic field lines accompanied by the outward ejection of accelerated electron beams (Joshi *et al.*, 2007, 2017). Notably, the post-flare loops following the first flare appear to be compact and low-lying (Figure 4e) whereas a large arcade of closed flare loops emerges only after the second phase of the eruption (Figure 4i). Many theoretical studies demonstrate the formation or emergence of magnetic flux ropes in solar active regions (Titov and Démoulin, 1999; Kliem, Titov, and Török, 2004; Archontis *et al.*, 2009; Kumar *et al.*, 2016; Prasad, Bhattacharyya, and Kumar, 2017). Notably, in compliance with the present observations, simulations by Prasad, Bhattacharyya, and Kumar (2017) showed asymmetric rise along with bifurcations of the flux rope during its ascent. The successful eruption of the flux rope leads to the transformation of the coronal active region from a sigmoid to an arcade morphology (Archontis *et al.*, 2009; Joshi *et al.*, 2017). The comparison between the kinematic evolution of the hot flux rope channel and associated CME reveals that the flux rope channel acts as the earliest signature of the CME in the source region (Cheng *et al.*, 2013; Patsourakos, Vourlidas, and Stenborg, 2013; Joshi *et al.*, 2016, 2017).

The Sun was very active during 18–25 June 2015 in producing geoeffective CMEs (Manoharan *et al.*, 2016). The CME on 21 June 2015 was a fast event with a linear projected speed of 1366 km s $^{-1}$ (Figure 5). It very likely interacted with preceding slow CMEs (see Section 3.4). Our study reveals many signatures of CME–CME interactions from radio data and *in situ* measurements. As described in the literature, the interaction of two or more CMEs exhibits complex phenomena, including magnetic reconnection, changes in the CME expansion, the propagation of a fast magnetosonic shock through a magnetic ejecta, and momentum exchange (Lugaz *et al.*, 2017). In the dynamic DH radio spectrum, the CME propagation is seen as an interplanetary type II shock starting from \approx 02:30 UT that continued up to \approx 05:30 UT in the frequency range of \approx 5–0.3 MHz (Figure 7). The most interesting part of the type II emission is the occurrence of intense patches of enhanced brightness superimposed on the main type II structure. A cluster of short-duration patches are observed during \approx 04:00–05:30 UT while relative longer and brighter patches are observed during \approx 07:30–9:00 UT (CME–CME interaction signatures are marked in Figure 7). This kind

of enhanced radio emission during type II bursts provides strong evidence for CME–CME interaction (Gopalswamy *et al.*, 2001b; Martínez Oliveros *et al.*, 2012; Shanmugaraju *et al.*, 2014; Temmer *et al.*, 2014; Lugaz *et al.*, 2017).

The effects of complex interactions between CMEs seem to have left its footprints at 1 AU (Figure 8). A low intensity shock precedes a major shock by ≈ 12 hours (marked by vertical lines 1 and 2 in Figure 8). Interestingly, shock 1 seems to indicate the arrival of a slow CME at 1 AU and brings in the decline in the Dst index. The arrival of a major CME-associated disturbance is marked by shock 2, which is followed by a dense sheath region. The *in situ* measurements clearly reveal two distinct MC structures (marked as MC I and MC II, Figure 8), which suggest that the structure evolved by the overtaking of successive CMEs (Wang, Ye, and Wang, 2003). Both DBM and ECA models validate the shock II and subsequent MCs to be the near-Earth counterpart of the solar flux rope eruption and flares observed on 21 June 2015 at $\approx 01:30$ – $03:00$ UT (Figures 2 and 4). However, it is to be noted that the ECA model calculation is close to the shock arrival time while the DBM estimation is more consistent with the MC arrival time (see Table 2). The speed profile indicates that the solar wind speed was gradually declining throughout the two MCs. The common sheath preceding the two MCs indicates that they interacted (Lugaz *et al.*, 2017). However, unlike *complex ejecta* defined by Burlaga, Plunkett, and St. Cyr (2002) as the case where two or more successive CMEs have merged so that individual MC characteristics are not visible anymore, in our event MC I and MC II are clearly identifiable which suggests interaction at the near-Earth region. The interaction region between MC I and MC II (shown between the dashed lines 4 and 5 in Figure 8) is characterized by abrupt changes in the magnetic field and plasma parameters, indicating the annihilation of the magnetic flux. The impulsive rise and fall of the proton temperature in this region further points towards localized magnetic reconnection as the two MCs interacted in the interplanetary medium. We attribute the structure identified in *in situ* measurements of the interaction region between the two MCs as a magnetic hole (Burlaga and Lemaire, 1978; Zurbuchen *et al.*, 2001; Sharma *et al.*, 2013). The interplanetary radio emission from *Wind*/WAVES clearly indicates signatures of CME–CME interaction between ≈ 10 – $90 R_{\odot}$ (Figure 7), while the CME height–time plots further suggest the scenario of interaction at even greater distances (Figure 6). Thus it is likely that a composite CME structure emerged after multiple interactions between the large CME on 21 June with several preceding slower events that mainly occurred on the previous day and after these interactions the individual CME structures were gradually lost. This composite CME structure interacted further with another halo CME that left the Sun on 19 June in the interplanetary medium, far-off from the Sun, thus giving rise to distinct MC structures separated by a magnetic hole. It is also likely that the magnetic structures of the two interacting CMEs did not favor a full merging by reconnection. From the near-Sun observations, interplanetary radio emissions, and *in situ* measurements at 1 AU, we identify complex processes of interaction right from the source active region to the corona and interplanetary medium that have significantly contributed to make this event so geoeffective.

6. Conclusions

The CME on 21 June 2015, ejected from AR NOAA 12371, was a major geoeffective event that led to a decrease in Dst of up to -204 nT. In this work, we provide a comprehensive multi-wavelength investigation of the CME from the source region, corona, and interplanetary medium along with its *in situ* signatures at 1 AU. The results of this study can be summarized as:

- The observations of AR 12371 reveal the pre-existence of a large EUV coronal sigmoid displaying intense emission in the 94 Å channel from its core region. Notably, the eruption initiated from the compact, magnetically bipolar region near the core which subsequently involved the full sigmoidal active region. Simultaneous with the pre-flare EUV brightening, multiple patches of enhanced emission were observed in H α in the vicinity of the filament. We attribute these pre-flare observations as evidence of tether-cutting reconnections occurring below the flux rope that subsequently triggered the CME initiation.
- The multi-wavelength observations of the active region clearly reveal the two-phase eruption of the hot flux rope, which accompanied the dual stages of standard flare reconnection. Thus, the magnetic reconnection during the two-phase eruption manifested in the form of two successive M-class flares.
- The eruption of flux ropes led to a fast halo CME with a linear speed of 1366 km s⁻¹. The study reveals clear signatures of CME–CME interactions in the corona and near-Sun region in the form of multiple continuum-like enhancements of decametric to hectometric type II radio emission. These features confirm that the fast CME moves through preceding slow CMEs.
- The *in situ* measurements confirm two distinct magnetic cloud structures separated by a magnetic hole. Our study reveals that complex, multiple structures of varying intensities associated with shocks and magnetic clouds contribute toward the enhancement of the geoeffectiveness of the solar eruption.

Acknowledgements We thank SDO, *Wind*/WAVES, and GONG teams for their open data policy. SDO is a NASA mission under the Living With a Star (LWS) program. The data services from CDAWeb are also thankfully acknowledged. We sincerely thank the anonymous referee for providing constructive comments and suggestions that have significantly enhanced the presentation and quality of the paper. We thank Prabir K. Mitra for help in AIA data analysis.

Disclosure of Potential Conflict of Interest The authors declare that they have no conflict of interest.

References

- Archontis, V., Hood, A.W., Savcheva, A., Golub, L., Deluca, E.: 2009, On the structure and evolution of complexity in sigmoids: A flux emergence model. *Astrophys. J.* **691**, 1276. DOI. ADS.
- Bamba, Y., Lee, K.-S., Imada, S., Kusano, K.: 2017, Study on precursor activity of the X1.6 flare in the great AR 12192 with SDO, IRIS, and Hinode. *Astrophys. J.* **840**, 116. DOI. ADS.
- Benz, A.O.: 2017, Flare observations. *Living Rev. Solar Phys.* **14**, 2. DOI. ADS.
- Bougeret, J.-L., Kaiser, M.L., Kellogg, P.J., Manning, R., Goetz, K., Monson, S.J., Monge, N., Friel, L., Meetre, C.A., Perche, C., Sitruk, L., Hoang, S.: 1995, Waves: The radio and plasma wave investigation on the Wind spacecraft. *Space Sci. Rev.* **71**, 231. DOI. ADS.
- Brueckner, G.E., Howard, R.A., Koomen, M.J., Korendyke, C.M., Michels, D.J., Moses, J.D., Socker, D.G., Dere, K.P., Lamy, P.L., Llebaria, A., Bout, M.V., Schwenn, R., Simnett, G.M., Bedford, D.K., Eyles, C.J.: 1995, The Large Angle Spectroscopic Coronagraph (LASCO). *Solar Phys.* **162**, 357. DOI. ADS.
- Burlaga, L.F., Lemaire, J.F.: 1978, Interplanetary magnetic holes – theory. *J. Geophys. Res.* **83**, 5157. DOI. ADS.
- Burlaga, L.F., Plunkett, S.P., St. Cyr, O.C.: 2002, Successive CMEs and complex ejecta. *J. Geophys. Res.* **107**, 1266. DOI. ADS.
- Burlaga, L., Sittler, E., Mariani, F., Schwenn, R.: 1981, Magnetic loop behind an interplanetary shock – Voyager, Helios, and IMP 8 observations. *J. Geophys. Res.* **86**, 6673. DOI. ADS.
- Canfield, R.C., Hudson, H.S., McKenzie, D.E.: 1999, Sigmoidal morphology and eruptive solar activity. *Geophys. Res. Lett.* **26**, 627. DOI. ADS.
- Chandra, R., Filippov, B., Joshi, R., Schmieder, B.: 2017, Two-step filament eruption during 14–15 March 2015. *Solar Phys.* **292**, 81. DOI. ADS.
- Cheng, X., Zhang, J., Liu, Y., Ding, M.D.: 2011, Observing flux rope formation during the impulsive phase of a solar eruption. *Astrophys. J. Lett.* **732**, L25. DOI. ADS.

- Cheng, X., Zhang, J., Ding, M.D., Liu, Y., Poomvises, W.: 2013, The driver of coronal mass ejections in the low corona: a flux rope. *Astrophys. J.* **763**, 43. DOI. ADS.
- Cheng, X., Ding, M.D., Zhang, J., Sun, X.D., Guo, Y., Wang, Y.M., Kliem, B., Deng, Y.Y.: 2014a, Formation of a double-decker magnetic flux rope in the sigmoidal solar active region 11520. *Astrophys. J.* **789**, 93. DOI. ADS.
- Cheng, X., Ding, M.D., Zhang, J., Srivastava, A.K., Guo, Y., Chen, P.F., Sun, J.Q.: 2014b, On the relationship between a hot-channel-like solar magnetic flux rope and its embedded prominence. *Astrophys. J. Lett.* **789**, L35. DOI. ADS.
- Dhara, S.K., Belur, R., Kumar, P., Banyal, R.K., Mathew, S.K., Joshi, B.: 2017, Trigger of successive filament eruptions observed by SDO and STEREO. *Solar Phys.* **292**, 145. DOI. ADS.
- Fletcher, L., Dennis, B.R., Hudson, H.S., Krucker, S., Phillips, K., Veronig, A., Battaglia, M., Bone, L., Caspi, A., Chen, Q., Gallagher, P., Grigis, P.T., Ji, H., Liu, W., Milligan, R.O., Temmer, M.: 2011, An observational overview of solar flares. *Space Sci. Rev.* **159**, 19. DOI. ADS.
- Gibson, S.E., Fan, Y.: 2006, Coronal prominence structure and dynamics: A magnetic flux rope interpretation. *J. Geophys. Res.* **111**, A12103. DOI. ADS.
- Glover, A., Ranns, N.D.R., Harra, L.K., Culhane, J.L.: 2000, The onset and association of CMEs with sigmoidal active regions. *Geophys. Res. Lett.* **27**, 2161. DOI. ADS.
- Gopalswamy, N., Lara, A., Yashiro, S., Kaiser, M.L., Howard, R.A.: 2001a, Predicting the 1-AU arrival times of coronal mass ejections. *J. Geophys. Res.* **106**, 29207. DOI. ADS.
- Gopalswamy, N., Yashiro, S., Kaiser, M.L., Howard, R.A., Bougeret, J.-L.: 2001b, Radio signatures of coronal mass ejection interaction: Coronal mass ejection cannibalism? *Astrophys. J. Lett.* **548**, L91. DOI. ADS.
- Joshi, B., Manoharan, P.K., Veronig, A.M., Pant, P., Pandey, K.: 2007, Multi-wavelength signatures of magnetic reconnection of a flare-associated coronal mass ejection. *Solar Phys.* **242**, 143. DOI. ADS.
- Joshi, B., Veronig, A.M., Lee, J., Bong, S.-C., Tiwari, S.K., Cho, K.-S.: 2011, Pre-flare activity and magnetic reconnection during the evolutionary stages of energy release in a solar eruptive flare. *Astrophys. J.* **743**, 195. DOI. ADS.
- Joshi, B., Kushwaha, U., Cho, K.-S., Veronig, A.M.: 2013, RHESSI and TRACE observations of multiple flare activity in AR 10656 and associated filament eruption. *Astrophys. J.* **771**, 1. DOI. ADS.
- Joshi, B., Kushwaha, U., Veronig, A.M., Cho, K.-S.: 2016, Pre-flare coronal jet and evolutionary phases of a solar eruptive prominence associated with the M1.8 flare: SDO and RHESSI observations. *Astrophys. J.* **832**, 130. DOI. ADS.
- Joshi, B., Kushwaha, U., Veronig, A.M., Dhara, S.K., Shanmugaraju, A., Moon, Y.-J.: 2017, Formation and eruption of a flux rope from the sigmoid active region NOAA 11719 and associated M6.5 flare: A multi-wavelength study. *Astrophys. J.* **834**, 42. DOI. ADS.
- Kilpua, E.K.J., Balogh, A., von Steiger, R., Liu, Y.D.: 2017, Geoeffective properties of solar transients and stream interaction regions. *Space Sci. Rev.* **212**, 1271. DOI. ADS.
- Kliem, B., Titov, V.S., Török, T.: 2004, Formation of current sheets and sigmoidal structure by the kink instability of a magnetic loop. *Astron. Astrophys.* **413**, L23. DOI. ADS.
- Kopp, R.A., Pneuman, G.W.: 1976, Magnetic reconnection in the corona and the loop prominence phenomenon. *Solar Phys.* **50**, 85. DOI. ADS.
- Krall, J., Sterling, A.C.: 2007, Analysis of erupting solar prominences in terms of an underlying flux-rope configuration. *Astrophys. J.* **663**, 1354. DOI. ADS.
- Kumar, S., Bhattacharyya, R., Joshi, B., Smolarkiewicz, P.K.: 2016, On the role of repetitive magnetic reconnections in evolution of magnetic flux ropes in solar corona. *Astrophys. J.* **830**, 80. DOI. ADS.
- Kushwaha, U., Joshi, B., Veronig, A.M., Moon, Y.-J.: 2015, Large-scale contraction and subsequent disruption of coronal loops during various phases of the M6.2 Flare associated with the confined flux rope eruption. *Astrophys. J.* **807**, 101. DOI. ADS.
- Leblanc, Y., Dulk, G.A., Bougeret, J.-L.: 1998, Tracing the electron density from the corona to 1 au. *Solar Phys.* **183**, 165. DOI. ADS.
- Lemen, J.R., Title, A.M., Akin, D.J., Boerner, P.F., Chou, C., Drake, J.F., Duncan, D.W., Edwards, C.G., Friedlaender, F.M., Heyman, G.F., Hurlburt, N.E., Katz, N.L., Kushner, G.D., Levay, M., Lindgren, R.W., Mathur, D.P., McFeaters, E.L., Mitchell, S., Rehse, R.A., Schrijver, C.J., Springer, L.A., Stern, R.A., Tarbell, T.D., Wuelser, J.-P., Wolfson, C.J., Yanari, C., Bookbinder, J.A., Cheimets, P.N., Caldwell, D., Deluca, E.E., Gates, R., Golub, L., Park, S., Podgorski, W.A., Bush, R.I., Scherrer, P.H., Gumm, M.A., Smith, P., Auker, G., Jerram, P., Pool, P., Soufli, R., Windt, D.L., Beardsley, S., Clapp, M., Lang, J., Waltham, N.: 2012, The Atmospheric Imaging Assembly (AIA) on the Solar Dynamics Observatory (SDO). *Solar Phys.* **275**, 17. DOI. ADS.
- Lepri, S.T., Zurbuchen, T.H.: 2010, Direct Observational evidence of filament material within interplanetary coronal mass ejections. *Astrophys. J. Lett.* **723**, L22. DOI. ADS.

- Liu, C., Lee, J., Yurchyshyn, V., Deng, N., Cho, K.-s., Karlický, M., Wang, H.: 2007, The eruption from a sigmoidal solar active region on 2005 May 13. *Astrophys. J.* **669**, 1372. DOI. ADS.
- Lugaz, N., Temmer, M., Wang, Y., Farrugia, C.J.: 2017, The interaction of successive coronal mass ejections: A review. *Solar Phys.* **292**, 64. DOI. ADS.
- Manoharan, P.K., van Driel-Gesztelyi, L., Pick, M., Demoulin, P.: 1996, Evidence for large-scale solar magnetic reconnection from radio and X-ray measurements. *Astrophys. J. Lett.* **468**, L73. DOI. ADS.
- Manoharan, P.K., Maia, D., Johri, A., Induja, M.S.: 2016, Interplanetary consequences of coronal mass ejection events occurred during 18–25 June 2015. In: Dorotovic, I., Fischer, C.E., Temmer, M. (eds.) *Coimbra Solar Physics Meeting: Ground-Based Solar Observations in the Space Instrumentation Era*, *Astron. Soc. Pacific Conf. Ser.* **504**, 59. ADS.
- Martínez Oliveros, J.C., Raftery, C.L., Bain, H.M., Liu, Y., Krupar, V., Bale, S., Krucker, S.: 2012, The 2010 August 1 type II burst: A CME–CME interaction and its radio and white-light manifestations. *Astrophys. J.* **748**, 66. DOI. ADS.
- Moore, R.L., Roumeliotis, G.: 1992, Triggering of eruptive flares – destabilization of the preflare magnetic field configuration. In: Svestka, Z., Jackson, B.V., Machado, M.E. (eds.) *IAU Colloq. 133: Eruptive Solar Flares, Lec. Notes Phys.* **399**, 69. DOI. ADS.
- Moore, R.L., Sterling, A.C., Hudson, H.S., Lemen, J.R.: 2001, Onset of the magnetic explosion in solar flares and coronal mass ejections. *Astrophys. J.* **552**, 833. DOI. ADS.
- Nindos, A., Patsourakos, S., Vourlidas, A., Tagikas, C.: 2015, How common are hot magnetic flux ropes in the low solar corona? A statistical study of EUV observations. *Astrophys. J.* **808**, 117. DOI. ADS.
- Patsourakos, S., Vourlidas, A., Stenborg, G.: 2013, Direct evidence for a fast coronal mass ejection driven by the prior formation and subsequent destabilization of a magnetic flux rope. *Astrophys. J.* **764**, 125. DOI. ADS.
- Pesnell, W.D., Thompson, B.J., Chamberlin, P.C.: 2012, The Solar Dynamics Observatory (SDO). *Solar Phys.* **275**, 3. DOI. ADS.
- Pevtsov, A.A.: 2002, Active-region filaments and X-ray sigmoids. *Solar Phys.* **207**, 111. ADS.
- Prasad, A., Bhattacharyya, R., Kumar, S.: 2017, Magnetohydrodynamic modeling of solar coronal dynamics with an initial non-force-free magnetic field. *Astrophys. J.* **840**, 37. DOI. ADS.
- Rust, D.M., Kumar, A.: 1996, Evidence for helically kinked magnetic flux ropes in solar eruptions. *Astrophys. J. Lett.* **464**, L199. DOI. ADS.
- Schmieder, B., Aulanier, G., Vršnak, B.: 2015, Flare-CME models: An observational perspective (invited review). *Solar Phys.* **290**, 3457. DOI. ADS.
- Schou, J., Scherrer, P.H., Bush, R.I., Wachter, R., Couvidat, S., Rabello-Soares, M.C., Bogart, R.S., Hoeksema, J.T., Liu, Y., Duvall, T.L., Akin, D.J., Allard, B.A., Miles, J.W., Rairden, R., Shine, R.A., Tarbell, T.D., Title, A.M., Wolfson, R.J., Elmore, D.F., Norton, A.A., Tomczyk, S.: 2012, Design and ground calibration of the Helioseismic and Magnetic Imager (HMI) Instrument on the Solar Dynamics Observatory (SDO). *Solar Phys.* **275**, 229. DOI. ADS.
- Shanmugaraju, A., Vršnak, B.: 2014, Transit time of coronal mass ejections under different ambient solar wind conditions. *Solar Phys.* **289**, 339. DOI. ADS.
- Shanmugaraju, A., Prasanna Subramanian, S., Vrsnak, B., Ibrahim, M.S.: 2014, Interaction between two CMEs during 14–15 February 2011 and their unusual radio signature. *Solar Phys.* **289**, 4621. DOI. ADS.
- Sharma, R., Srivastava, N., Chakrabarty, D., Möstl, C., Hu, Q.: 2013, Interplanetary and geomagnetic consequences of 5 January 2005 CMEs associated with eruptive filaments. *J. Geophys. Res.* **118**, 3954. DOI. ADS.
- Shibata, K.: 1999, Evidence of magnetic reconnection in solar flares and a unified model of flares. *Astrophys. Space Sci.* **264**, 129. DOI. ADS.
- Syed Ibrahim, M., Shanmugaraju, A., Bendict Lawrance, M.: 2015, Transit time of CME/shock associated with four major geo-effective CMEs in solar cycle 24. *Adv. Space Res.* **55**, 407. DOI. ADS.
- Temmer, M., Veronig, A.M., Peinhart, V., Vršnak, B.: 2014, Asymmetry in the CME–CME interaction process for the events from 2011 February 14–15. *Astrophys. J.* **785**, 85. DOI. ADS.
- Titov, V.S., Démoulin, P.: 1999, Basic topology of twisted magnetic configurations in solar flares. *Astron. Astrophys.* **351**, 707. ADS.
- Vourlidas, A., Lynch, B.J., Howard, R.A., Li, Y.: 2013, How many CMEs have flux ropes? Deciphering the signatures of shocks, flux ropes, and prominences in coronagraph observations of CMEs. *Solar Phys.* **284**, 179. DOI. ADS.
- Vršnak, B., Žic, T., Vrbanec, D., Temmer, M., Rollett, T., Möstl, C., Veronig, A., Čalogović, J., Dumbović, M., Lulić, S., Moon, Y.-J., Shanmugaraju, A.: 2013, Propagation of interplanetary coronal mass ejections: The drag-based model. *Solar Phys.* **285**, 295. DOI. ADS.
- Wang, Y.M., Ye, P.Z., Wang, S.: 2003, Multiple magnetic clouds: Several examples during March–April 2001. *J. Geophys. Res.* **108**, 1370. DOI. ADS.

- Zhao, X., Dryer, M.: 2014, Current status of CME/shock arrival time prediction. *Space Weather* **12**, 448. [DOI](#). [ADS](#).
- Zurbuchen, T.H., Richardson, I.G.: 2006, In-situ solar wind and magnetic field signatures of interplanetary coronal mass ejections. *Space Sci. Rev.* **123**, 31. [DOI](#). [ADS](#).
- Zurbuchen, T.H., Hefi, S., Fisk, L.A., Gloeckler, G., Schwadron, N.A., Smith, C.W., Ness, N.F., Skoug, R.M., McComas, D.J., Burlaga, L.F.: 2001, On the origin of microscale magnetic holes in the solar wind. *J. Geophys. Res.* **106**, 16001. [DOI](#). [ADS](#).